ADVANCED MATERIALS
www.advmat.de

Ion and Molecular Sieving With Ultrathin Polydopamine Nanomembranes

Jiyao Yu, Tommaso Marchesi D'Alvise, Iain Harley, Adam Krysztofik, Ingo Lieberwirth, Przemyslaw Pula, Pawel W. Majewski, Bartlomiej Graczykowski, Johannes Hunger, Katharina Landfester, Seah Ling Kuan, Rachel Shi, Christopher V. Synatschke, and Tanja Weil**

In contrast to biological cell membranes, it is still a major challenge for synthetic membranes to efficiently separate ions and small molecules due to their similar sizes in the sub-nanometer range. Inspired by biological ion channels with their unique channel wall chemistry that facilitates ion sieving by ion-channel interactions, the first free-standing, ultrathin (10–17 nm) nanomembranes composed entirely of polydopamine (PDA) are reported here as ion and molecular sieves. These nanomembranes are obtained via an easily scalable electropolymerization strategy and provide nanochannels with various amine and phenolic hydroxyl groups that offer a favorable chemical environment for ion-channel electrostatic and hydrogen bond interactions. They exhibit remarkable selectivity for monovalent ions over multivalent ions and larger species with K^+/Mg^{2+} of ≈4.2, $K^+/[Fe(CN)_6]^{3-}$ of ≈10.3, and K^+/Rhodamine B of ≈273.0 in a pressure-driven process, as well as cyclic reversible pH-responsive gating properties. Infrared spectra reveal hydrogen bond formation between hydrated multivalent ions and PDA, which prevents the transport of multivalent ions and facilitates high selectivity. Chemically rich, free-standing, and pH-responsive PDA nanomembranes with specific interaction sites are proposed as customizable high-performance sieves for a wide range of challenging separation requirements.

1. Introduction

Industrially relevant ion sieving applications, such as flow batteries,[1,2] desalination,[3] and energy conversion,[4] involve the separation of certain ionic species from complex mixtures under harsh conditions, which require robust membranes with increased ion selectivity.[5] However, as ions have very similar sizes in the sub-nanometer (sub-nm) range, achieving an efficient ion sieving performance remains a great challenge. Ultrathin crystalline porous materials such as graphene, graphene oxide,[6] and metal/covalent organic frameworks,[7,8] provide rigid sub-nm channels, as well as high permeability, making them, in principle, ideal for such applications. However, large cracks and crystalline defects (i.e., inter- and intracrystalline defects)[9] in these materials limit the reproducibility of their properties, making scale-up challenging.[10–12] In addition, they currently lack stability as they swell or

J. Yu, T. Marchesi D'Alvise, S. L. Kuan, R. Shi, C. V. Synatschke, T. Weil
Synthesis of Macromolecules
Max Planck Institute for Polymer Research
Ackermannweg 10, 55128 Mainz, Germany
E-mail: synatschke@mpip-mainz.mpg.de; weil@mpip-mainz.mpg.de

I. Harley, I. Lieberwirth, K. Landfester
Physical Chemistry of Polymers
Max Planck Institute for Polymer Research
Ackermannweg 10, 55128 Mainz, Germany

The ORCID identification number(s) for the author(s) of this article can be found under https://doi.org/10.1002/adma.202401137

DOI: 10.1002/adma.202401137

A. Krysztofik, B. Graczykowski
Faculty of Physics
Adam Mickiewicz University
Uniwersytetu Poznanskiego 2, 61-614 Poznan, Poland

P. Pula, P. W. Majewski
Department of Chemistry
University of Warsaw
Ludwika Pasteura 1, 02-093 Warsaw, Poland

J. Hunger
Molecular Spectroscopy
Max Planck Institute for Polymer Research
Ackermannweg 10, 55128 Mainz, Germany

deform in organic solvents or acid/alkaline environments.[13–15] There is therefore a lack of materials with rigid pores that can be processed like polymers, easily forming defect-free continuous membranes and having excellent chemical and mechanical stabilities.

In addition to conventional separation, which is simply based on pore size, new transport pathways, for example, via interactions with functionalities embedded in the membranes, would have to be identified and utilized to further improve ion selectivity. During evolution, biological cell membranes with their unique channel wall chemistry have emerged. These membranes provide local fine-tuned polarity for selective electrostatic and hydrogen bonding interactions, so that, they can intelligently control ion transport across the membrane, providing a sophisticated prototype for membrane design.[16,17] Although the molecular mechanisms by which biological membranes function are better understood, the development of such excellent ion-sieving polymeric membranes is still a challenge as they can only interact with ions to a limited extent. New polymeric materials with a variety of ion-channel interaction sites are needed.

Mussel-inspired polydopamine (PDA), which is formed by the oxidation of dopamine, is considered to be biocompatible, environmentally friendly, and easily functionalized due to many reactive groups.[18,19] It exhibits amphoteric properties due to the presence of amine groups and catechol groups,[20–22] which could be useful for the preparation of smart ion sieving membranes that respond to pH changes. The presence of various hydrogen bonding sites in PDA could also contribute to ion selectivity[23] as theoretical simulations have demonstrated that hydrated divalent cations have to overcome higher energy barriers than monovalent cations during transport across the membrane due to hydrogen bonds.[24] In addition, PDA is a highly crosslinked polymeric network,[25] which is insoluble in nearly all organic solvents.[26] We therefore envision robust PDA membranes that enable intelligent ion sieving, as well as responding to pH stimuli, through hydrogen bonding and electrostatic interactions. However, to achieve this challenge, membranes with uniform and nm-sized pores have to be created. While PDA is widely used as a functional coating on a substrate membrane,[27–29] there are only a few examples of ultrathin PDA membranes with controlled thickness or pore size.[30,31] Recently, we reported a series of ultrathin, homogenous, robust, and free-standing polymeric films prepared by electropolymerization that had contributed to solving the long-standing challenge of reproducibly fabricating polymeric films with precisely controllable and ultrathin geometries.[32–35]

Herein, we report the fabrication of the first ultrathin (10–17 nm) defect-free nanomembranes composed of pure PDA via an easily scalable electropolymerization strategy. By transferring the PDA membranes onto track-etched polycarbonate (PC) membranes, we fabricate continuous membranes exhibiting a significantly higher K^+/RB selectivity of ≈273.0 compared to previous membranes in a pressure-driven process.[36,37] Infrared spectra suggest that, compared with monovalent ions, hydrated multivalent ions are more likely to bind to hydrogen bonding sites inside the membrane channels, which can prevent the transport of these ions and explain the excellent selectivity of the membranes toward monovalent ions. Further, the gating performance of the PDA membrane can be rapidly and reversibly manipulated by adjusting the pH, further allowing us to separate binary dye mixtures with similar molecular sizes but different charge characteristics. We envision that our approach can afford advanced biomimetic membranes based on multiple sieving mechanisms for ion sieving and ionic energy conversion.

2. Results and Discussion

2.1. Fabrication and Characterization of PDA Nanomembranes

For the preparation of the freestanding PDA nanomembranes, electropolymerization approaches using a standard three-electrode electrochemical cell (**Figure 1B**) operated either in cyclic voltammetry (CV, Figure 1A) or pulsed deposition (PD, Figure 1C) process were used.[33,34] We have shown previously that both processes allow fast deposition times to obtain PDA films with programmable thickness and geometry, high homogeneity, and mechanical strength. More interestingly, they lead to differences in the cross-link of PDA membranes, which may affect the sieving performance of these membranes.

For the CV process, the PDA layer (CV membrane) was grown by sweeping the potential between −0.5 and +0.5 V with various cycle numbers (5, 10, and 15) (Figure 1A). In the first positive CV scan (Figure 1D), an oxidative peak emerged at 0.25 V, which was related to the oxidation of catechol to quinone. This molecule underwent cyclization to leucodopaminechrome, and then, oxidation to dopaminechrome, followed by further oxidation and cyclization reactions leading to the formation of a highly crosslinked PDA membrane (Figure S1, Supporting Information).[38,39] As depicted in Figure 1C,E, for PD, the PDA layer (PD membrane) was obtained by the following pulse cycles: +0.5 V/2 s; 0 V/2 s; −0.3 V/2 s; and 0 V/3 s (100, 150, and 200 pulse cycles). Similar to the CV deposition, in which peak current decreased sharply for the first five cycles, an exponential decrease throughout 100 pulses was observed. This indicates the formation of an insulating PDA layer, which was also reflected in the thickness variation, as shown in Figure 1G; Figure S2, Supporting Information.

To obtain PDA membranes with comparable thickness from PD and CV for better comparison of their sieving performance, the fabrication parameters, especially cycle numbers were optimized. The thickness of both membranes increased linearly in the range of 10–17 nm with a growth rate of 0.6 nm per CV or ten PD cycles until an insulating layer was formed. This allowed the thickness of the resulting membranes to be precisely tailored by electrochemical deposition, a feature that was difficult to achieve by conventional synthetic routes.[40–43] In addition, the PDA membrane electropolymerized onto the gold substrate appeared highly homogeneous with a very low mean roughness of ≈2.0 ± 0.1 nm (Figure 1F,H; Figure S3, Supporting Information).

PDA membranes prepared on the gold substrates could be easily removed using a method established before,[33] where a sacrificial polyvinyl alcohol (PVA) layer was used as a mechanical support. Subsequently, PDA membranes could be transferred onto porous supports without defects by applying the surface tension-assisted vacuum filtration transfer method (**Figure 2A**; Figure S4, Supporting Information). Before performing ion and molecular sieving studies, the PDA membrane was transferred onto a porous hydrophilic, track-etched PC support membrane

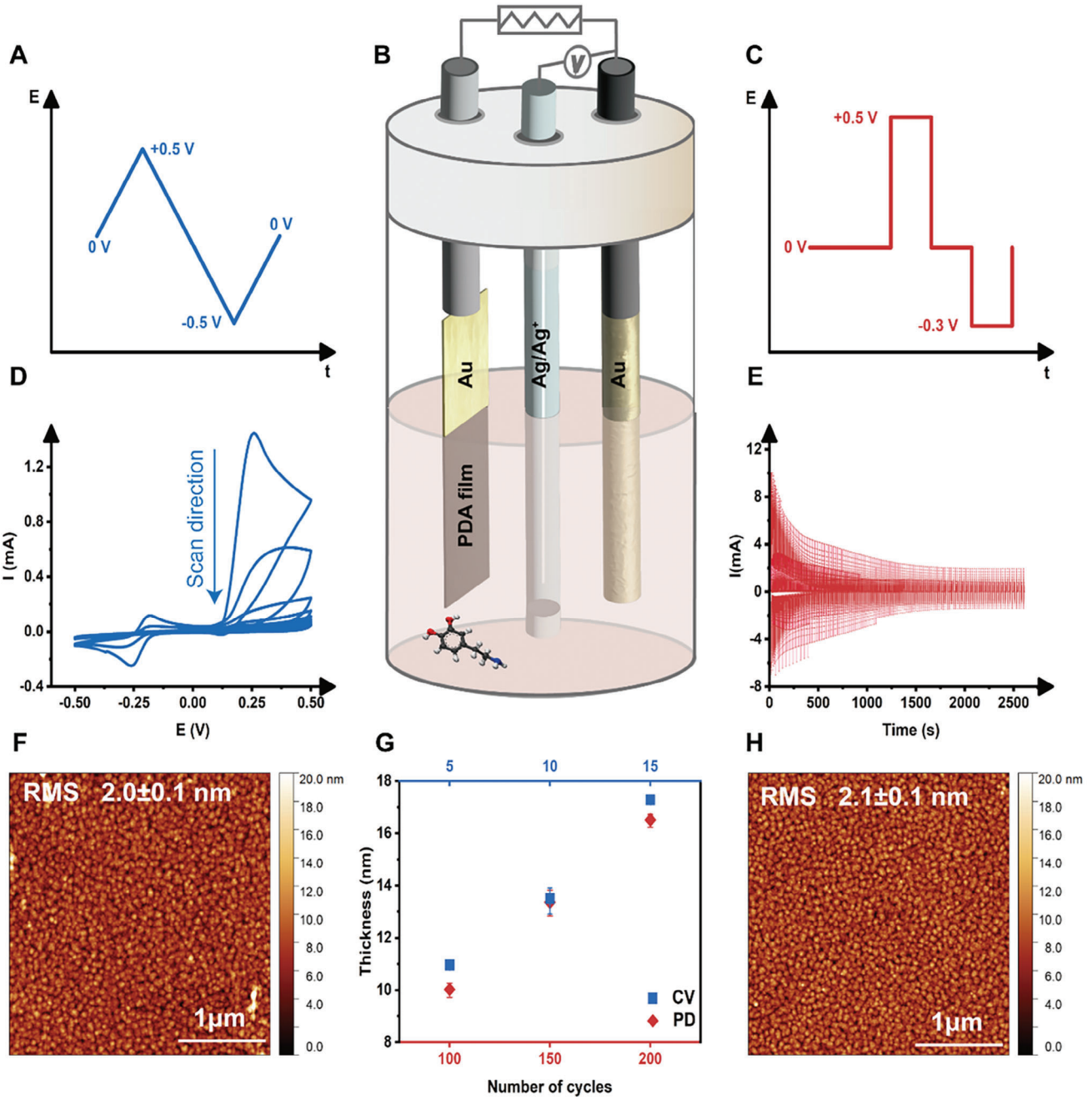

Figure 1. PDA membrane preparation via electropolymerization. A) Electropolymerization schematic for the CV process. B) Schematic diagram of the setup for electropolymerization. C) Electropolymerization schematic for the PD process. D) CV profiles of the electropolymerization process recorded for ten scan cycles. E) PD profiles of the electropolymerization process recorded for 150 pulse cycles. F) Atomic force microscopy (AFM) image of the CV10c PDA membrane on Au substrate. RMS, root mean square. G) PDA membrane thickness as a function of the number of cycles of PDA membranes. H) AFM image of the PD150c PDA membrane on Au substrate.

(Figure S5, Supporting Information) to form a composite membrane. Hydrophilic PC membranes were used due to their well-defined isolated cylindrical pores (220 nm diameter), smooth surface, and good adhesion to PDA membranes. The resulting membranes are referred to hereafter as CV/PDXc_PC, where PD or CV refers to the electropolymerization process used for PDA synthesis and Xc is the cycle number.

Next, we analyzed the membranes by scanning electron microscopy (SEM), transmission electron microscopy (TEM), micro-Brillouin light scattering spectroscopy (μ-BLS), X-ray reflectometry (XRR), contact angle (CA) measurements, X-ray photoelectron spectroscopy (XPS), and Fourier transform infrared spectroscopy (FTIR). The transferred PDA membrane retained its structural integrity with no obvious holes or tears up

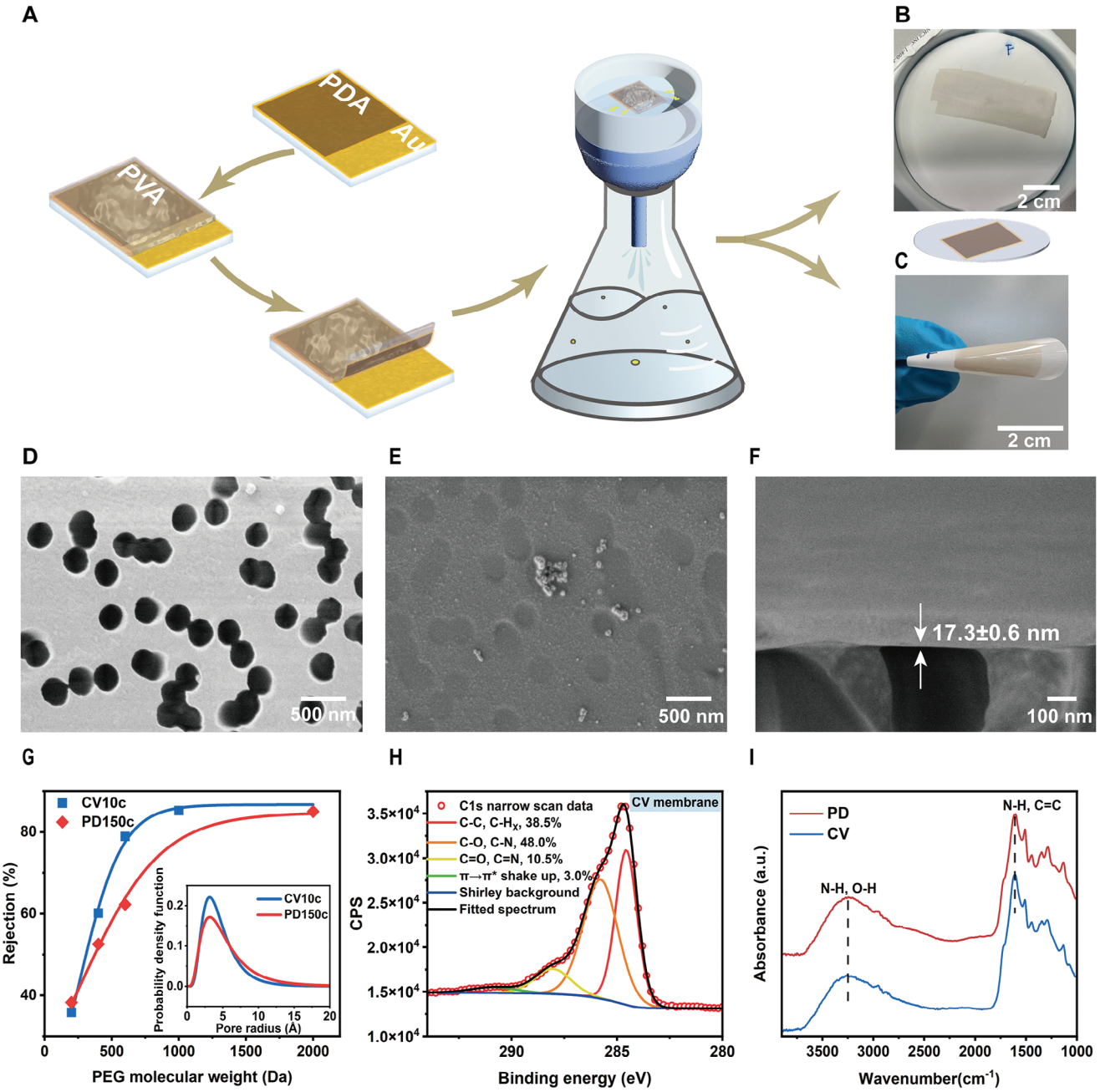

Figure 2. PDA membrane transfer process and characterization. A) Schematic representation of the PDA membrane transfer process. B) Photograph of the composite membrane CV10c_nylon with a dimension of 15 cm^2. C) Photograph of the flexible composite membrane CV10c_PC with a dimension of 2.5 cm^2. D) SEM top-view image of bare track-etched PC membrane with a pore size of 220 nm. E) SEM top-view image of CV15c_PC membrane. F) SEM cross-section image of CV15c_PC membrane with a PDA layer of 17.3 ± 0.6 nm thickness. G) Rejection data in % of CV10c_PC and PD150c_PC membranes measured by rejecting PEG with different molecular weights. Inset: pore size distribution derived from the rejection curves of PEG. H) High-resolution narrow scan of C1s of CV10c PDA membrane on the gold substrate and the deconvoluted spectra for the probable chemical species. I) FTIR spectra of both CV15c and PD200c PDA membranes on gold substrate.

to dimensions of 15 cm^2 (Figure 2B,C), which was confirmed by high-resolution SEM (Figure 2E; Figure S6, Supporting Information). Due to its ultrathin thickness of 17.3 ± 0.6 nm for CV15c (Figure 2F), the prepared PDA membrane exhibited high transparency; so that, the underlying PC membrane (Figure 2D) was still visible. High-resolution TEM images revealed the presence of nm-sized pores (Figure S7, Supporting Information). By rejecting neutral solutes of polyethylene glycol (PEG, Table S1, Supporting Information) with different molecular weights, the obtained pore size distributions (Figure 2G) further verified nm-pores, in which the average pore sizes for CV10c and PD150c were 8.3 Å and 9.2 Å, respectively. Tomography (Figure S8,

Supporting Information) of the CV10c PDA membrane showed that the membrane thickness was in the range of ≈10 nm, in good agreement with the AFM data.

It is worth noting that both PDA membranes were mechanically robust and flexible. An outstandingly high Young's modulus between 7 and 10.5 GPa was measured for CV membranes by contactless and non-invasive μ-BLS at GHz frequency; while, PD membranes had an even higher Young's modulus between 8.2 and 11.2 GPa (Figure S9, Supporting Information), most likely due to the denser and highly crosslinked structure of the PD membranes compared to the CV membranes, as confirmed by density measurement via XRR (Figure S10, Supporting Information). We attribute the decrease in Young's modulus after five cycles for CV and 100 cycles for PD to a less dense material deposition, which was in line with the obtained electrochemical data (Figure 1D,E) and density data (Figure S10, Supporting Information). Note that the modulus of conventional PDA films was ≈2 GPa, and the highest modulus of polyamide films reported so far was 3.57 GPa,[44,45] when determined via strain-induced elastic buckling instability for mechanical measurements by transferring the films onto a stretched polydimethylsiloxane elastomer.[46] CA measurements on the PDA membranes revealed the advancing water CA was in the range of 37.6–62.0°, indicating that the membranes were hydrophilic in nature (Figure S11, Supporting Information).

The chemical structure of both types of PDA membranes was characterized by XPS and FTIR analysis, and no obvious functional group differences between the CV and PD membranes were observed. High-resolution C1s XPS (Figure 2H; Figure S12 and Tables S2 and S3, Supporting Information) indicated that the PDA membrane was mainly composed of C—C/C—H_x and C—O/C—N with an abundance ratio of 48.0%, which was slightly higher compared to other reported PDA films (25–40%).[25,47] In FTIR spectroscopy studies (Figure 2I), the broad peak from 3200 to 3450 cm^{-1} was assigned to the stretching vibrations of O—H and N—H in catecholamine. Further, the characteristic stretching vibration of the aromatic ring and bending vibration of N—H were observed at 1602 cm^{-1}, indicating the existence of an indole ring and confirming the successful polymerization of dopamine hydrochloride.[48]

2.2. Selective Ion and Molecular Transport Through PDA Membranes

Using a pressure-driven process (Figure S13, Supporting Information),[49] we demonstrated that both CV_PC and PD_PC membranes exhibit high ion and molecular sieving performance (**Figure 3**) for a wide range of ions and dye molecules with different hydrated diameters and charges (Table S4, Supporting Information). The pressure-driven process is of greater practical importance but requires the material to be more robust to withstand the required pressures than the more commonly reported concentration-driven process.[50–53]

First, the impact of membrane thickness (cycle number) on the water permeance and methyl orange (MO) rejection properties was investigated (Figure 3A,B; Figure S14, Supporting Information). Water permeance initially decreased with the cycle number (up to 10 cycles for CV and 150 cycles for PD membrane), and then, became constant; while, the opposite trends were observed for MO rejection. This indicated the formation of a structurally stable membrane already at 10 CV cycles or 150 PD cycles, and these membranes were selected for further analysis.

As shown in Figure 3C, the CV10c_PC membrane showed a sharp rejection curve where the membranes display a distinctive selectivity of monovalent ions over multivalent ions and larger species. Specifically, the rejection rates of the CV10c_PC membrane followed the sequence of RB > $[Ru(NH_3)_6]^{3+}$, MnB, MO, $[Fe(CN)_6]^{3-}$, Al^{3+}, Fe^{3+} > Mg^{2+} > Ca^{2+} >> Li^+ > Na^+ > K^+ > H^+, indicating an apparent sharp cutoff channel size of ≈ 8 Å, which was smaller than the measured CV10c_PC membrane average channel size of ≈ 8.3 Å (Figure 2G). A similar sieving trend (Figure S15, Supporting Information) was observed for the PD150c_PC membrane with an average channel size of 9.2 Å. These data suggest that rather than a simple size-dependent separation mechanism controlling the ion transport, additional interactions such as electrostatic and hydrogen bonding interactions between the membrane channel and the metal ions play an important role in determining the performance of the membranes.

Membrane rejection values for monovalent ions such as H^+, K^+, Na^+, and Li^+ were 8.1 ± 5.0%, 13.6 ± 1.7%, 14.9 ± 2.8%, and 15.0 ± 1.1%, respectively; while, for larger ions and molecules such as MO, MnB, and $[Ru(NH_3)_6]^{3+}$, rejection values were calculated to be higher than 94%, and for RB, it was up to 99.7%. Therefore, the membrane exhibited excellent selectivities for K^+/Mg^{2+} of ≈4.2, $K^+/[Fe(CN)_6]^{3-}$ of ≈10.3, Na^+/RB of ≈268.7, and K^+/RB of ≈273.0 (Figure 3D), which were much higher than selectivities reported previously for state-of-the-art membranes (Figure 3E; Table S5, Supporting Information). Compared with the CV10c_PC membrane, lower rejections/selectivities and higher permeance were observed for PD150c_PC, which could be well explained by their structural differences (Figure 3F; Figure S15, Supporting Information). In addition, the PDA membrane permeance and rejection performance were found to be exceptionally stable over time (Figure S16, Supporting Information), and its structural integrity after the 24 h filtration test was further confirmed by SEM (Figure S17, Supporting Information). The PDA membranes were also insoluble in nearly all organic solvents,[26] such as non-polar hexane and polar methanol solution, and retained their structural integrity even after 30 days (Figure S18, Supporting Information), demonstrating their great potential for organic solvent nanofiltration.

2.3. Electrostatic Interactions Improve the Ion and Molecular Sieving Performance

Due to the presence of amine and catechol groups, the charge of the channel wall of the PDA membrane depends on the environmental pH. We measured an isoelectric point of the CV10c_PC membrane of ≈4.2 by zeta potential measurement, indicating that the channels hold a net neutral charge at this pH (Figure S19, Supporting Information). At pH below 4.2, the channels will be positively charged because of the protonation of the amino groups; while, at pH above 4.2, negatively charged channels exist due to the deprotonation of the catechol radicals. We hypothesized that the charge of the channel wall could influence its

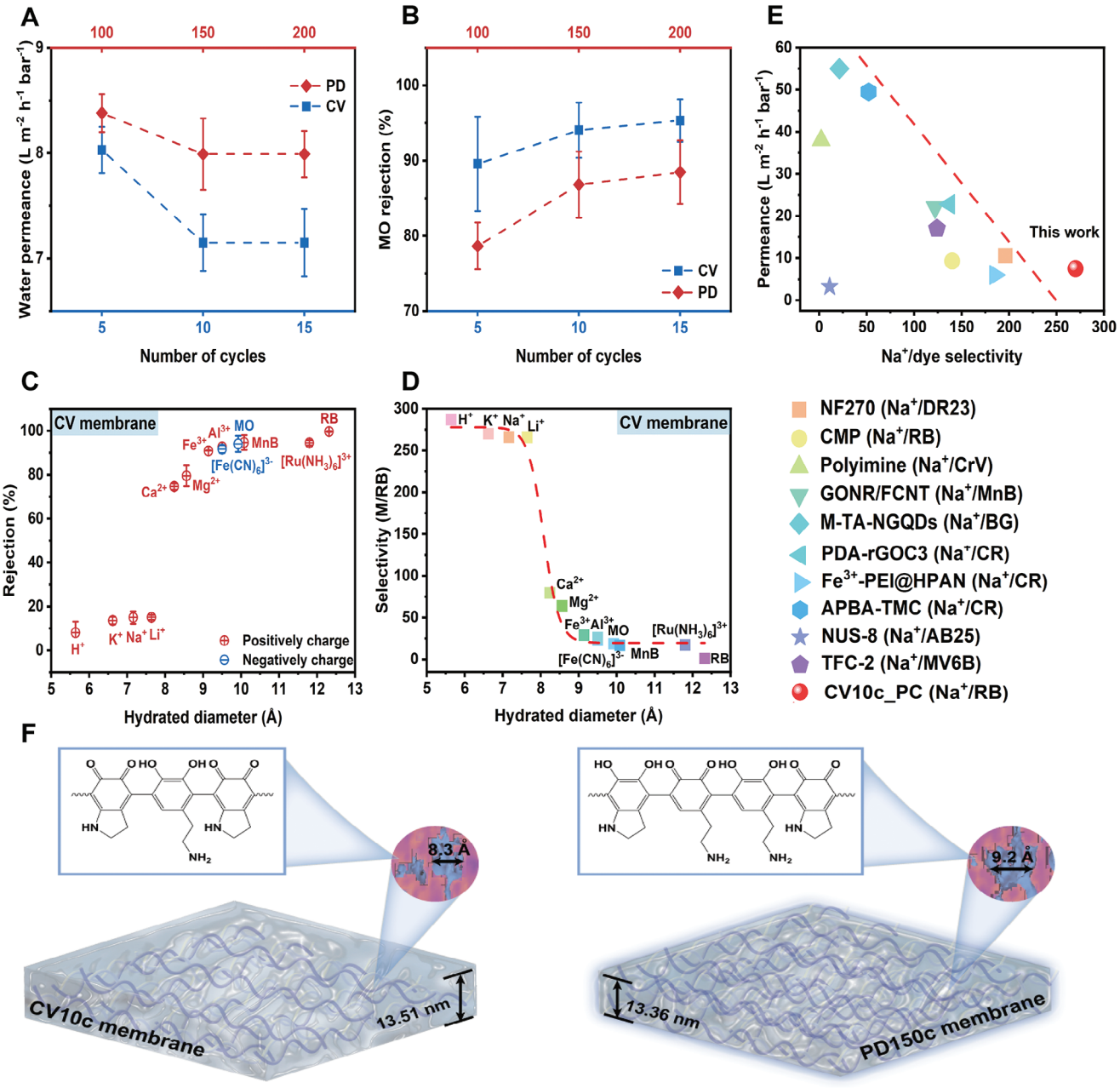

Figure 3. Ion and molecular sieving performance of PDA membranes. A) Water permeance for both PDA membranes with different scan cycles. B) MO rejection for both PDA membranes with different scan cycles. C) Rejection performance of CV10c_PC membrane, as a function of hydrated diameter, for probe ions and molecules with different charges and sizes. MO is methyl orange, MnB is methylene blue, and RB is rhodamine B. D) Selectivity (ions or molecules to RB) of CV10c_PC membrane versus hydrated diameter. E) Typical Na^+/dye separation data of state-of-the-art ion-selective membranes such as polymers, graphene-oxide, conjugated microporous polymer membranes, PDA-modified membranes, and commercialized Nafion membranes that are reported in the literature (Table S5, Supporting Information). DR23 is direct red 23, CrV is crystal violet, BG is brilliant green, CR is congo red, AB25 is acid blue 25, and MV6B is methyl violet 6B. The red dashed line is added manually to show the trade-off effect between selectivity and permeance. F) Schematic comparison between CV10c membrane and PD150c membrane. Compared with the CV10c membrane, PD150c membrane is denser, has a larger average pore size, and broader pore size distribution, and has more hydrophilic functional groups per area.

electrostatic interactions with ions and charged molecules, which would in turn affect the sieving performance. Therefore, we investigated the possibility of tuning the sieving performance of PDA membranes against ions and charged molecules via pH control.

The CV10c_PC membrane was selected to elucidate the transport mechanisms as the PD150c_PC membrane showed similar chemical groups and sieving performance. We selected three representative pH values (pH 2, 6, and 9) to assess the pH-responsive gating performance of the PDA membranes. At pH 2, the

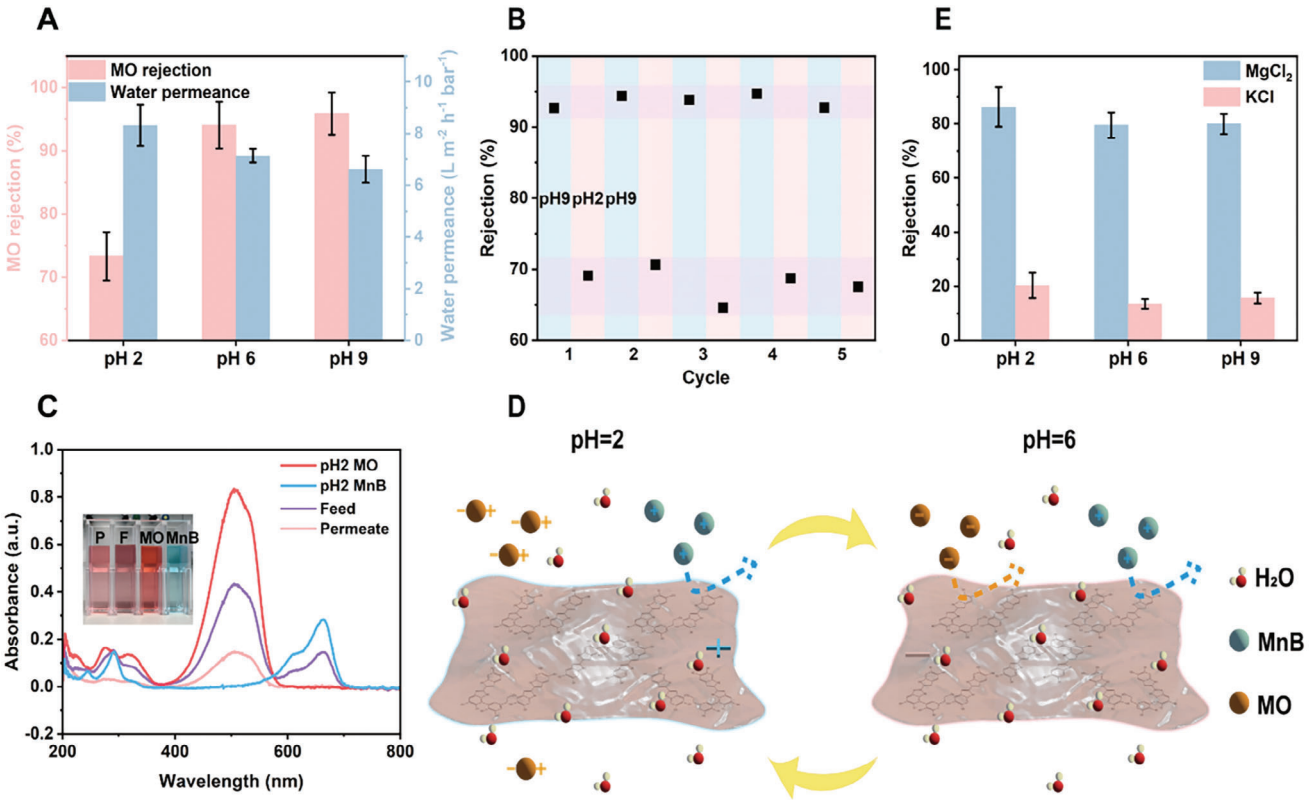

Figure 4. Effect of the electrostatic interactions on the ion and molecular sieving performance. A) Impact of the pH on the pure water permeance and MO rejection of the CV10c_PC membrane. B) Cyclic reversibility of MO rejection of the CV10c_PC membrane when the pH was shifted from 9 to 2 and back to 9 for five cycles. C) UV–vis spectra of the pH 2 MO, pH 2 MnB, the feed solution (1:1 mixture of pH 2 MO and pH 2 MnB), and the permeate collected after 24 h filtration. Separation of the binary dye mixture was performed by a CV10c_PC membrane through a dead-end filtration cell. The specific absorbance peak for MO at pH 2 was 507 nm; while, it was 664 nm for MnB. D) Schematic illustration of pH-responsive gating channels. E) Effects of pH on the monovalent (K^+) and divalent (Mg^{2+}) ions rejection of CV10c_PC membrane.

channel wall was positively charged, whereas at pH 6 and 9, the channel wall became negatively charged. Note that pH 6 was the original pH of 20 ppm MO solution. As shown in **Figure** 4A, the rejection of MO increased significantly with increasing pH from 2 (73.3 ± 3.9%) to 6 (94.1 ± 3.7%), and then, reached a rejection plateau above pH 6 (95.9 ± 3.3%); while, the opposite trend was observed for water permeance (pH 2: 8.3 ± 0.8 L m^{-2} h^{-1} bar^{-1}, pH 6: 7.1 ± 0.3 L m^{-2} h^{-1} bar^{-1}, pH 9: 6.6 ± 0.5 L m^{-2} h^{-1} bar^{-1}). No obvious swelling behavior difference at different pH was observed by surface plasmon resonance measurements, which excluded the effect of structural difference caused by swelling on the sieving performance (Figure S20, Supporting Information). Hence, these properties were most likely due to the positively charged channels that exerted a lower electrostatic attraction on the zwitterionic MO at lower pH values,[54] which facilitated the transport of MO. In contrast, at higher pH, the negatively charged channels showed electrostatic repulsion toward MO, which reduced the transport of MO. These results indicate that PDA membranes have excellent pH-dependent gating properties.

Next, we investigated the dynamic cyclic reversibility of MO rejection responding to the pH that was varied from 9 to 2 and back to 9 for five cycles. As shown in Figure 4B, the MO rejection reached 64.5–72.0% at pH 2 and 92.7–94.3% at pH 9, indicating a strong, stable, and cyclic reversible pH-responsive gating performance, making the PDA membranes interesting materials for smart gating applications, and possibly, as sensors.

The observation of such a strong pH-dependent gating behavior allowed us to manipulate the separation of differently charged binary dye mixtures, even of dyes of comparable molecular sizes and structures, which is normally difficult to achieve by simply adjusting the ambient pH. To demonstrate this, we separated MO from a MO and MnB mixture by adjusting the pH to 2. Initially, a pH 2 water feedstock containing MO (M_w = 327.3 Da, 9.92 Å, zwitterionic at pH 2) and MnB (M_w = 319.9 Da, 10.08 Å, positively charged) with a concentration ratio of 1:1 was filtered through the CV10c_PC membrane. The permeates collected after 24 h filtration were light red (Figure 4C), which already indicated that only MO was transported through the membrane, whereas MnB was blocked. This was confirmed by the UV–vis analysis, in which the feed solution showed both MO and MnB characteristic peaks; while, the permeate solution showed only the MO peak (Figure 4C). In general, different electrostatic interactions due to the change in charge were the main reason for the selective dye sieving. In this respect, the negatively charged channels were closed for both MO and MnB, at pH 6, whereas the positively charged channels were open for amphoteric MO (68.1%) due to weakened electrostatic interaction but remained closed for positively charged MnB (≈100%, Figure S21, Supporting

Information) at pH 2; see Figure 4D. However, the rejection of Mg^{2+} versus K^+ was hardly affected by the change in pH (Figure 4E), suggesting that the observed high selectivity of PDA membranes for monovalent ions over multivalent ions and larger molecules may be due to molecular mechanisms other than electrostatic interactions.

2.4. Hydrogen Bonds Between Hydrated Ions and the PDA Membrane Channels are Responsible for Ion-Selective Sieving

The PDA membrane channels contain potential hydrogen bonding sites, as indicated by the presence of N—H and O—H bands in the FTIR characterization shown in Figure 2I. Therefore, metal ions surrounded by their hydration shells can form hydrogen bonds with these hydrogen bonding sites in the channels of the PDA membrane.[55] To gain further insight into the mechanism of selective sieving of monovalent ions over multivalent ions, humidity-controlled FTIR spectra of the PDA membrane were measured after incubation with different ions (monovalent Na^+, multivalent Mg^{2+}, and Ca^{2+}) to further analyze the interaction between hydrated metal ions and hydrogen bonding sites along the channels of the PDA membrane.

The FTIR spectra are dominated by O—H and N—H stretching bands at 3200–3450 cm^{-1} and rich spectral features at < 1650 cm^{-1}, where C=C stretching, N—H bending, and also H_2O bending vibrations contribute. With increasing humidity, the raw spectra exhibit a minor shift of the peak at 1602 cm^{-1} (presumably N—H bending), and the broad O—H/N—H stretching peaks at 3200–3450 cm^{-1}, together with an increasing absorbance at ≈1630 cm^{-1} and 3200–3450 cm^{-1}, indicative of water uptake and hydrogen bond formation between water and PDA membrane (**Figures** 5A,B and 5C, respectively).

To isolate the effect of water uptake in the vibrational spectra, we calculated difference spectra (spectra at a given humidity−spectrum in N_2 atmosphere), normalized to the maximum of the O—H stretching band at 3200–3450 cm^{-1}, which are displayed in Figure 5D–F. These difference spectra were dominated by positive bands at 3475 and 1630 cm^{-1}, which could be explained by the O—H stretching band and the H_2O bending vibration of absorbed water. Intensity ratios at 3260 cm^{-1} relative to 3450 cm^{-1} for PDA+Na^+ and PDA+Ca^{2+} were lower as compared to pure PDA, indicating that the ions altered the line shape of the O—H stretching band of water in the channels.[56,57] In addition, we observed a negative band in these differential spectra at ≈1735 cm^{-1} for PDA and for PDA+Na^+ (Figure 5D,E), which could be explained by a peak shift of the vibrational modes of PDA. With increasing humidity, absorbed water formed hydrogen bonds with PDA (presumably with the N—H groups), which resulted in a shift of PDA vibrations. Such spectral shifts gave rise to positive and negative features in the difference spectra. Remarkably, for the membrane incubated with Ca^{2+}, this negative feature was nearly absent (Figure 5F), indicating that most of the hydrogen bonding sites along the membrane channels had been occupied with hydrated Ca^{2+}. As such, excess adsorbed water did not form hydrogen bonds to PDA for PDA+Ca^{2+}, in contrast to PDA+Na^+. Membranes incubated with Mg^{2+} also showed a result similar to PDA+Ca^{2+} (Figure S22, Supporting Information). Therefore, it is likely that hydrated multivalent ions were more favored to form hydrogen bonds with hydrogen bonding sites along the membrane channels, compared to monovalent metal ions. Such PDA–ion interaction explains the ion selectivity of PDA membranes toward monovalent ions, consistent with simulations that suggest that divalent ions engaged in hydrogen bonding interactions are required to overcome higher energy barriers for their transport across the membrane.[24]

3. Conclusion

In summary, inspired by the unique channel wall chemistry of biological cell membranes, we demonstrate the first example of ultrathin, efficient sieving membranes made of PDA, with strong electrostatic and hydrogen bonding interactions through electropolymerization. In particular, the electropolymerization strategy results in high uniformity of sub-2-nm pores, and abundant hydrogen bonding sites provide stronger hydrogen bond interactions between hydrated multivalent ions and the channels to facilitate the permeation of monovalent ions, resulting in competitive selectivities for K^+/Mg^{2+} of ≈4.2, $K^+/[Fe(CN)_6]^{3-}$ of ≈10.3, and K^+/RB of ≈273.0. In addition, these amphoteric PDA membranes exhibit reversible pH-responsive gating properties, allowing for efficient separation of binary dye mixtures of similar molecular size but different charges. Considering the remarkable sieving performance for monovalent ions, we anticipate that our strategy will provide new avenues for future developments of biomimetic advanced membranes based on multiple-sieving mechanisms for promising applications such as highly efficient ion separation and ionic energy conversion.

While the current preparation process, which requires a transfer step, has limitations for industrial applications, it is conceivable that a more scalable production method can be developed using an automated lifting procedure or by using porous substrates directly as working electrodes in electropolymerization. We envision that future efforts will focus on introducing interaction sites into the membranes to design PDA sieving membranes that target specific ions.

4. Experimental Section

Preparation of PDA Membranes Via Electropolymerization: Electropolymerization of CV and PD PDA membranes on gold substrates was performed using a Metrohm Autolab Nseries potentiostat (AUTOLAB PGSTAT 204) connected with a standard three-electrode electrochemical cell. An Ag/AgCl (3 M KCl) electrode, commercially available gold-coated glass, and gold wire were used as reference electrode, working electrode, and counter electrode, respectively. Before use, gold working electrodes were cleaned using acetone, Milli-Q water, and argon plasma cleaning. Dopamine hydrochloride (1 mg mL^{-1}) was dissolved in (100 mM) phosphate buffer (pH 7.0) and purged for at least 15 min with nitrogen to remove dissolved oxygen to obtain a homogeneous electrolyte solution. The CV process was performed from −0.5 V to 0.5 V at a scan rate of 0.01 V s^{-1}; while, the PD membranes were obtained by scanning the following pulse cycles: 0.5 V/2 s, 0 V/2 s, −0.3 V/2 s, and 0 V/3 s.

Transfer Process of PDA Membranes onto Support: First, the PDA membrane on the gold substrate was immersed in carbonate buffer (100 mM, pH 10) for 30 min at room temperature for further crosslinking of the dopamine monomers and oligomers. Second, three additional removal cycles between −0.8 and 1.2 V were applied to reduce the adhesion between the PDA membrane and the gold substrate. Then, the micrometer-thick

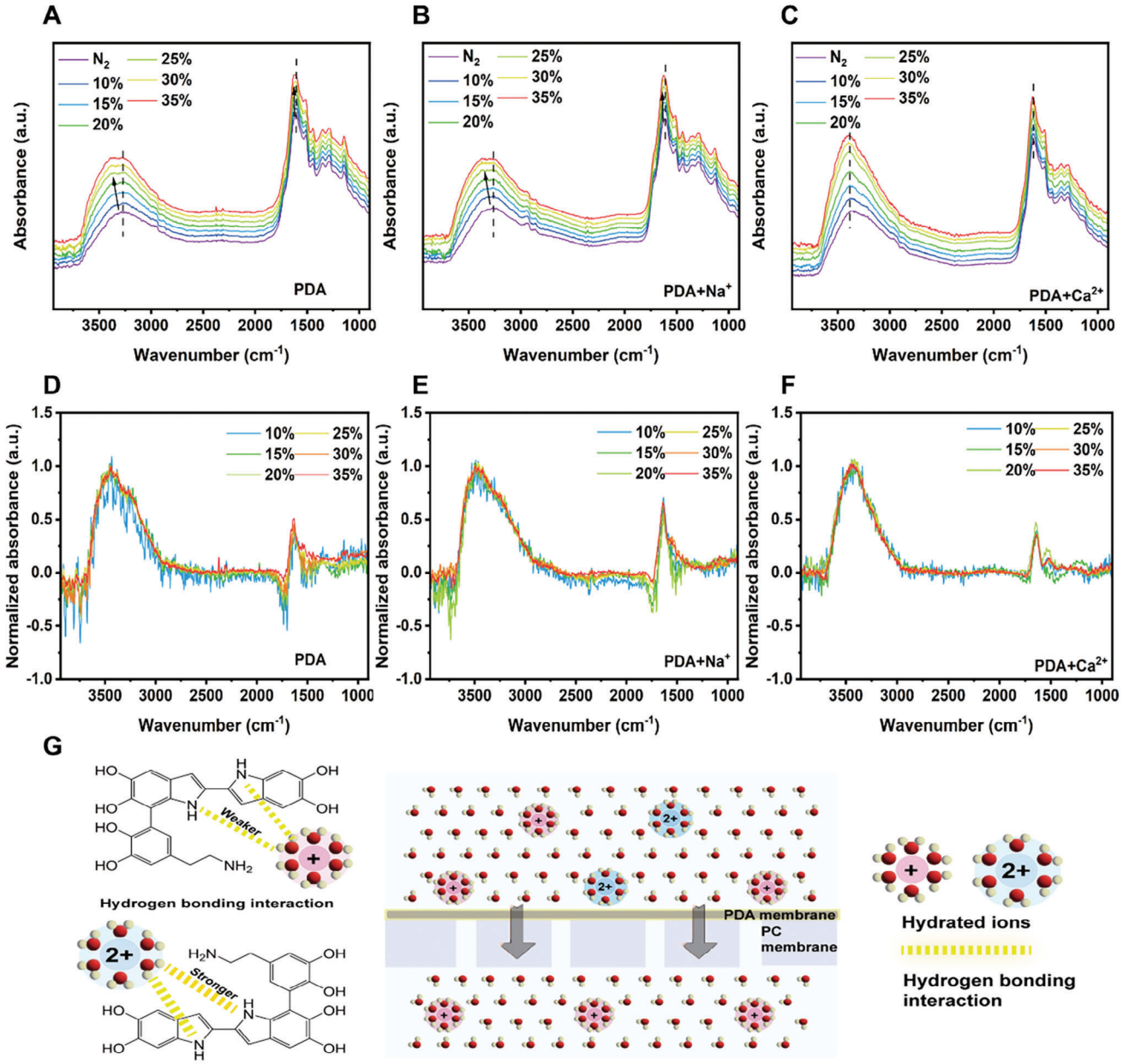

Figure 5. Mechanism of mono versus multivalent ions selective sieving. A) FTIR spectra of pure CV15c membrane, B) CV15c membrane after incubation with 1 g L^{-1} NaCl solution, and C) CV15c membrane after incubation with 1 g L^{-1} $CaCl_2$ solution under N_2 and air atmosphere with controlled humidity between 10% and 35%. Spectra revealed the uptake of water and provide indications for the hydrogen bond formation of water to the membrane. D–F) Spectra at different humidities with the spectrum under the N_2 atmosphere subtracted and a constant background subtracted. These difference spectra were normalized to the O—H stretching band of water. All different spectra showed positive signatures due to water uptake (O—H stretching and H_2O bending vibration). PDA (D) and PDA+Na^+ (E) spectra exhibited a negative feature at 1738 cm^{-1}, suggesting a shift of PDAs vibrations upon hydrogen bonding to water. This negative feature was absent for PDA+Ca^{2+}. G) Schematic illustration of the possible mechanism for ions transport across the membrane.

sacrificial PVA layer that serves as a mechanical support for membrane transfer was coated on the surface of the PDA membrane on the gold substrate by drop casting (200 µL, 10% in water) and then dried at 40 °C for ≈25 min. Subsequently, the PDA membrane was peeled off the gold substrate completely along with the PVA layer. The PDA/PVA layer could float on the water surface due to surface tension; while, transferring it into Milli-Q water. Finally, the PDA membrane was transferred onto the respective support by vacuum filtration and the PVA layer was gradually dissolved in water. After the transfer process, the sample was washed in water for 1 h to completely remove the PVA, and subsequently, dried at room temperature.

Characterization of the PDA Nanomembranes: The surface roughness and thickness of the PDA nanomembranes were characterized by AFM (Park NX20 and Bruker Dimension ICON, Germany). The surface morphologies of the membranes were analyzed by SEM (LEO Gemini 1530,

Carl Zeiss AG, Germany). A Titan Krios G4 Cryo-TEM (Thermo Fisher Scientific, USA) with a Gatan K3 detector and a 20 eV energy filter was used to assess the membrane pore structure and perform the tomography. Solute transport experiments were performed to determine the pore size of membranes using PEG with different molecular weights. The PEG concentrations in the feed and permeate solutions were quantified by liquid chromatography-mass spectrometry (LC-MS 2020, Shimadzu, Duisburg, Germany). The Young's modulus of the membranes was analyzed by μ-BLS at GHz frequencies. The advancing CA measurement was conducted using a Dataphysics OCA35 goniometer (Dataphysics, Germany). The chemical structures of the PDA membranes were further analyzed by XPS (Kratos Axis UltraDLD spectrometer 3, England) and FTIR (Vertex 70, Bruker, Germany). Fiber optic surface plasmon resonance was used for investigating the swelling behavior of the CV10c PDA membrane at different pH conditions. The surface charges of the membranes were measured by streaming potential over a pH range of 2–9 with an electrokinetic analyzer using a Cylindrical Cell (Anton-Paar SurPass3, Austria). The concentration of the organic dyes in the feed and permeate solutions was obtained by UV–vis spectrometry to quantify the rejected dye molecules; while, the ion centration was recorded by a conductivity portable meter (Orion Star A222, Thermo Fisher Scientific, USA) and Inductively Coupled Plasma Optical Emission Spectrometer (ICP-OES, Spectrogreen, Spectro, Germany) to quantify the ion sieving performance. Additional experimental details of the PDA membrane characterization are provided in the Supporting Information.

Membrane Performance Tests: The permeance and rejection capacity of the PDA membranes were measured using a dead-end filtration device with an effective area of 0.2827 cm^2 under a pressure difference of 2 bar at room temperature. There was a stirring bar rotating at 330 rpm within the filtration cell to avoid concentration polarization. For each performance test, 25 mL Milli-Q water was used to first test the pure water permeance of the membranes. Then, different salt or organic dye solutions were studied. The results were provided as average values from at least three membranes with statistical errors calculated by the STDEV function. The 0.5 mL dead volume downstream of the membrane inside the filtration cell was not prefilled, and the permeate filling took ≈2 h. The permeance was recorded every 10 min after it reached a steady state, which was typically observed within 30 min after the permeate flowed out. The permeance P (L m^{-2} h^{-1} bar^{-1}) was calculated according to Equation (1):

$$P = \frac{V}{At\Delta p} \tag{1}$$

where V (L) is the volume of permeate collected, A (m^2) is the effective membrane area, t (h) is the permeation time, and Δp (bar) is the applied pressure.

A series of 25 mL of inorganic salt and dye solutions, including HCl, KCl, NaCl, LiCl, $CaCl_2$, $MgCl_2$, $AlCl_3$, $FeCl_3$, $K_3[Fe(CN)_6]$, $[Ru(NH_3)_6]Cl_3$, MnB, MO, and RB, with concentrations of 1000 ppm (for salts) and 20 ppm (for dyes) in water was used as feed solution, respectively. To maintain an approximately constant solute concentration in the feed solution during each measurement, the total permeate flowing out of the filtration cell was set to less than 3 mL. The permeates were collected every 2 h and the rejection was also recorded after the steady state was achieved. The solute rejection R (%) was calculated using Equation (2):

$$R\ (\%) = \left(1 - \frac{C_p}{C_f}\right) \times 100\% \tag{2}$$

where C_p and C_f are the concentrations of the permeate and feed solutions, respectively.

The selectivity of solute A over solute B, α, was calculated using Equation (3):

$$\alpha = \frac{1 - R_A}{1 - R_B} \tag{3}$$

where R_A and R_B are the rejections of solutes A and B, respectively. Membrane stability tests, pH-responsive tests, reversible filtration tests, and binary dye mixture separation experiments are presented in the Supporting Information.

Supporting Information

Supporting Information is available from the Wiley Online Library or from the author.

Acknowledgements

The authors gratefully acknowledge funding by the Deutsche Forschungsgemeinschaft (DFG – German Research Foundation) – project number 364549901 – TRR 234 (CataLight B04 and Z02). J.Y. is grateful for the support from the China Scholarship Council. I.H. is thankful for the funding support from the H2020 Marie Curie Actions Fellowship of the European Commission (ITN SUPERCOL, grant agreement 860914). A.K. and B.G. acknowledge the National Science Centre of Poland (NCN) by the OPUS grant 2021/41/B/ST5/03038. The authors thank Detlev–Walter Scholdei for assisting with the FTIR measurements, Gunnar Glasser for investigating the morphology of the PDA membranes by using SEM, Leon Prädel for XPS measurement, and Sabrina Brand for conducting the ICP-OES measurements, as well as Yongkang Wang and Marcel Boecker for helpful scientific discussions.

Open access funding enabled and organized by Projekt DEAL.

Conflict of Interest

The authors declare no conflict of interest.

Author Contributions

J.Y. and T.M.D. conceived the idea. J.Y. conducted the experiments, analyzed the data, and wrote the manuscript. I.H., A.K., I.L., P.P., P.W.M., B.G., S.L.K., and R.S. performed the characterizations. J.Y., T.M.D., I.H., A.K., I.L., P.P., P.W.M., B.G., J.H., K.L., C.V.S., and T.W. discussed the results and commented on the manuscript. The manuscript was written through the contributions of all authors. All authors have approved the final version of the manuscript.

Data Availability Statement

The data that support the findings of this study are openly available in Zenodo repository at https://doi.org/10.5281/zenodo.11234402.

Keywords

ion sieving, nanomembranes, pH-responsive, polydopamine, precise separation, transport mechanisms

Received: January 22, 2024
Revised: May 3, 2024
Published online: May 23, 2024

[1] P. Zuo, Y. Li, A. Wang, R. Tan, Y. Liu, X. Liang, F. Sheng, G. Tang, L. Ge, L. Wu, Q. Song, N. B. McKeown, Z. Yang, T. Xu, *Angew. Chem., Int. Ed.* **2020**, *59*, 9564.

[2] R. Tan, A. Wang, R. Malpass-Evans, R. Williams, E. W. Zhao, T. Liu, C. Ye, X. Zhou, B. P. Darwich, Z. Fan, L. Turcani, E. Jackson, L. Chen, S. Y. Chong, T. Li, K. E. Jelfs, A. I. Cooper, N. P. Brandon, C. P. Grey, N. B. McKeown, Q. Song, *Nat. Mater.* **2020**, *19*, 195.
[3] S. P. Surwade, S. N. Smirnov, I. V. Vlassiouk, R. R. Unocic, G. M. Veith, S. Dai, S. M. Mahurin, *Nat. Nanotechnol.* **2015**, *10*, 459.
[4] A. Siria, P. Poncharal, A.-L. Biance, R. Fulcrand, X. Blase, S. T. Purcell, L. Bocquet, *Nature* **2013**, *494*, 455.
[5] R. Epsztein, R. M. DuChanois, C. L. Ritt, A. Noy, M. Elimelech, *Nat. Nanotechnol.* **2020**, *15*, 426.
[6] M. Zhang, P. Zhao, P. Li, Y. Ji, G. Liu, W. Jin, *ACS Nano* **2021**, *15*, 5209.
[7] J. Lu, H. Zhang, J. Hou, X. Li, X. Hu, Y. Hu, C. D. Easton, Q. Li, C. Sun, A. W. Thornton, M. R. Hill, X. Zhang, G. Jiang, J. Z. Liu, A. J. Hill, B. D. Freeman, L. Jiang, H. Wang, *Nat. Mater.* **2020**, *19*, 767.
[8] L. Cao, I. C. Chen, C. Chen, D. B. Shinde, X. Liu, Z. Li, Z. Zhou, Y. Zhang, Y. Han, Z. Lai, *J. Am. Chem. Soc.* **2022**, *144*, 12400.
[9] F. Dorosti, L. Ge, H. Wang, Z. Zhu, *Prog. Mater. Sci.* **2023**, *137*, 101123.
[10] B. Sengupta, Q. Dong, R. Khadka, D. K. Behera, R. Yang, J. Liu, J. Jiang, P. Keblinski, G. Belfort, M. Yu, *Science* **2023**, *381*, 1098.
[11] F. Banhart, J. Kotakoski, A. V. Krasheninnikov, *ACS Nano* **2011**, *5*, 26.
[12] H. Dou, M. Xu, B. Wang, Z. Zhang, G. Wen, Y. Zheng, D. Luo, L. Zhao, A. Yu, L. Zhang, Z. Jiang, Z. Chen, *Chem. Soc. Rev.* **2021**, *50*, 986.
[13] Z. Wang, C. Ma, C. Xu, S. A. Sinquefield, M. L. Shofner, S. Nair, *Nat. Sustain.* **2021**, *4*, 402.
[14] L. Huang, J. Chen, T. Gao, M. Zhang, Y. Li, L. Dai, L. Qu, G. Shi, *Adv. Mater.* **2016**, *28*, 8669.
[15] C. Wu, L. Xia, S. Xia, B. Van der Bruggen, Y. Zhao, *Small* **2023**, *19*, 2206041.
[16] B. Hille, C. M. Armstrong, R. MacKinnon, *Nat. Med.* **1999**, *5*, 1105.
[17] B. Corry, M. Thomas, *J. Am. Chem. Soc.* **2012**, *134*, 1840.
[18] W. Cheng, X. Zeng, H. Chen, Z. Li, W. Zeng, L. Mei, Y. Zhao, *ACS Nano* **2019**, *13*, 8537.
[19] Q. Huang, J. Chen, M. Liu, H. Huang, X. Zhang, Y. Wei, *Chem. Eng. J.* **2020**, *387*, 124019.
[20] Q. Liu, B. Yu, W. Ye, F. Zhou, *Macromol. Biosci.* **2011**, *11*, 1227.
[21] B. Yu, J. Liu, S. Liu, F. Zhou, *Chem. Commun.* **2010**, *46*, 5900.
[22] N. Schweigert, A. J. B. Zehnder, R. I. L. Eggen, *Environ. Microbiol.* **2001**, *3*, 81.
[23] W. Zhang, Y. Ying, J. Ma, X. Guo, H. Huang, D. Liu, C. Zhong, *J. Membr. Sci.* **2017**, *527*, 8.
[24] F. Sheng, B. Wu, X. Li, T. Xu, M. A. Shehzad, X. Wang, L. Ge, H. Wang, T. Xu, *Adv. Mater.* **2021**, *33*, 2104404.
[25] H. Hemmatpour, O. De Luca, D. Crestani, M. C. A. Stuart, A. Lasorsa, P. C. A. van der Wel, K. Loos, T. Giousis, V. Haddadi-Asl, P. Rudolf, *Nat. Commun.* **2023**, *14*, 664.
[26] P. Delparastan, K. G. Malollari, H. Lee, P. B. Messersmith, *Angew. Chem., Int. Ed.* **2019**, *58*, 1077.
[27] H. Yang, Y. Lan, W. Zhu, W. Li, D. Xu, J. Cui, D. Shen, G. Li, *J. Mater. Chem.* **2012**, *22*, 16994.
[28] L. Shao, Z. X. Wang, Y. L. Zhang, Z. X. Jiang, Y. Y. Liu, *J. Membr. Sci.* **2014**, *461*, 10.
[29] Z. Liu, Y. Hu, *ACS Appl. Mater. Interfaces* **2016**, *8*, 21666.
[30] J. Szewczyk, V. Babacic, A. Krysztofik, O. Ivashchenko, M. Pochylski, R. Pietrzak, J. Gapiński, B. Graczykowski, M. Bechelany, E. Coy, *ACS Appl. Mater. Interfaces* **2023**, *15*, 36922.
[31] X. Liu, H. Peng, J. Lu, Y. Ji, S. Li, J. Yuan, Q. Zhao, C. Gao, *Adv. Membr.* **2023**, *3*, 100059.
[32] T. Marchesi D'Alvise, S. Sunder, R. Hasler, J. Moser, W. Knoll, C. V. Synatschke, S. Harvey, T. Weil, *Macromol. Rapid Commun.* **2023**, *44*, 2200332.
[33] T. Marchesi D'Alvise, S. Harvey, L. Hueske, J. Szelwicka, L. Veith, T. P. J. Knowles, D. Kubiczek, C. Flaig, F. Port, K. E. Gottschalk, F. Rosenau, B. Graczykowski, G. Fytas, F. S. Ruggeri, K. Wunderlich, T. Weil, *Adv. Funct. Mater.* **2020**, *30*, 2000378.
[34] J. Kund, S. Daboss, T. M. D'Alvise, S. Harvey, C. V. Synatschke, T. Weil, C. Kranz, *Nanomaterials* **2021**, *11*, 1964.
[35] B. Stöckle, D. Y. W. Ng, C. Meier, T. Paust, F. Bischoff, T. Diemant, R. J. Behm, K.-E. Gottschalk, U. Ziener, T. Weil, *Macromol. Symp.* **2014**, *346*, 73.
[36] Z. Zhou, D. Guo, D. B. Shinde, L. Cao, Z. Li, X. Li, D. Lu, Z. Lai, *ACS Nano* **2021**, *15*, 11970.
[37] P. Li, Z. Wang, L. Yang, S. Zhao, P. Song, B. Khan, *J. Membr. Sci.* **2018**, *555*, 56.
[38] M. D. Hawley, S. V. Tatawawadi, S. Piekarski, R. N. Adams, *J. Am. Chem. Soc.* **1967**, *89*, 447.
[39] X.-L. Wen, Y.-H. Jia, Z.-L. Liu, *Talanta* **1999**, *50*, 1027.
[40] J.-E. Gu, S. Lee, C. M. Stafford, J. S. Lee, W. Choi, B.-Y. Kim, K.-Y. Baek, E. P. Chan, J. Y. Chung, J. Bang, J.-H. Lee, *Adv. Mater.* **2013**, *25*, 4778.
[41] P. M. Johnson, J. Yoon, J. Y. Kelly, J. A. Howarter, C. M. Stafford, *J. Polym. Sci. Part B: Polym. Phys.* **2012**, *50*, 168.
[42] K. C. Krogman, J. L. Lowery, N. S. Zacharia, G. C. Rutledge, P. T. Hammond, *Nat. Mater.* **2009**, *8*, 512.
[43] J. Zhao, F. Pan, P. Li, C. Zhao, Z. Jiang, P. Zhang, X. Cao, *ACS Appl. Mater. Interfaces* **2013**, *5*, 13275.
[44] L. Klosterman, Z. Ahmad, V. Viswanathan, C. J. Bettinger, *Adv. Mater Interfaces* **2017**, *4*, 1700041.
[45] Z. Jiang, S. Karan, A. G. Livingston, *Adv. Mater.* **2018**, *30*, 1705973.
[46] C. M. Stafford, C. Harrison, K. L. Beers, A. Karim, E. J. Amis, M. R. VanLandingham, H.-C. Kim, W. Volksen, R. D. Miller, E. E. Simonyi, *Nat. Mater.* **2004**, *3*, 545.
[47] E. Coy, I. Iatsunskyi, J. C. Colmenares, Y. Kim, R. Mrówczyński, *ACS Appl. Mater. Interfaces* **2021**, *13*, 23113.
[48] H. Lee, S. M. Dellatore, W. M. Miller, P. B. Messersmith, *Science* **2007**, *318*, 426.
[49] L. Prozorovska, P. R. Kidambi, *Adv. Mater.* **2018**, *30*, 1801179.
[50] R. K. Joshi, P. Carbone, F. C. Wang, V. G. Kravets, Y. Su, I. V. Grigorieva, H. A. Wu, A. K. Geim, R. R. Nair, *Science* **2014**, *343*, 752.
[51] J. Abraham, K. S. Vasu, C. D. Williams, K. Gopinadhan, Y. Su, C. T. Cherian, J. Dix, E. Prestat, S. J. Haigh, I. V. Grigorieva, P. Carbone, A. K. Geim, R. R. Nair, *Nat. Nanotechnol.* **2017**, *12*, 546.
[52] C. E. Ren, K. B. Hatzell, M. Alhabeb, Z. Ling, K. A. Mahmoud, Y. Gogotsi, *J. Phys. Chem. Lett.* **2015**, *6*, 4026.
[53] J. Wang, Z. Zhang, J. Zhu, M. Tian, S. Zheng, F. Wang, X. Wang, L. Wang, *Nat. Commun.* **2020**, *11*, 3540.
[54] Y. Akama, A. Tong, M. Ito, S. Tanaka, *Talanta* **1999**, *48*, 1133.
[55] B. Corry, *M.R.S. Bull.* **2017**, *42*, 306.
[56] R. Li, Z. Jiang, S. Shi, H. Yang, *J. Mol. Struct.* **2003**, *645*, 69.
[57] Q. Sun, *Vib. Spectrosc.* **2012**, *62*, 110.